

Quantum Criticality by Interaction Frustration in a Square-Planar Lattice

Yi-Qiang Lin,^{1,*} Chang-Chao Liu,¹ Jia-Xin Li,¹ Bai-Jiang Lv,² Kai-Xin Ye,³ Jia-Wen Zhang,³ Si-Qi Wu,⁴ Ya-Nan Zhang,³ Ye Chen,³ Jia-Yi Lu,¹ Jing Li,¹ Hua-Xun Li,¹ Hao Li,² Yi Liu,⁵ Cao Wang,⁶ Yun-Lei Sun,⁷ Hao Jiang,⁸ Hui-Qiu Yuan,^{3,9,10,11} and Guang-Han Cao^{1,10,11,12,†}

¹*School of Physics, Zhejiang University, Hangzhou 310058, China*

²*Key Laboratory of Neutron Physics and Institute of Nuclear Physics and Chemistry, China Academy of Engineering Physics, Mianyang, Sichuan 621999, China*

³*Center for Correlated Matter, School of Physics, Zhejiang University, Hangzhou 310058, China*

⁴*Department of Physics, The Hong Kong University of Science and Technology, Clear Water Bay, Hong Kong, China*

⁵*Department of Applied Physics, Key Laboratory of Quantum Precision Measurement of Zhejiang Province, Zhejiang University of Technology, Hangzhou, China*

⁶*School of Physics and Optoelectronic Engineering, Shandong University of Technology, Zibo, 255000, Shandong, China*

⁷*School of Information and Electrical Engineering, Hangzhou City University, Hangzhou, 310015, Zhejiang, China*

⁸*School of Physics and Optoelectronics, Xiangtan University, Xiangtan 411105, China*

⁹*Institute for Advanced Study in Physics, Zhejiang University, Hangzhou 310058, China*

¹⁰*Institute of Fundamental and Transdisciplinary Research, Zhejiang University, Hangzhou 310058, China*

¹¹*State Key Laboratory of Silicon and Advanced Semiconductor Materials, Zhejiang University, Hangzhou 310058, China*

¹²*Collaborative Innovation Center of Advanced Microstructures, Nanjing University, Nanjing, 210093, China*

We report experimental and theoretical investigations on $\text{ThCr}_2\text{Ge}_2\text{C}$, a metallic compound in which Cr_2C planes form a square-planar lattice. Neutron powder diffraction, magnetization, and specific heat measurements reveal no evidence of long-range magnetic order or short-range spin freezing down to 70 mK. Quantum critical behavior was indicated through logarithmic divergences in both the magnetic susceptibility and the specific heat divided by temperature. Resistivity measurements exhibit non-Fermi-liquid behavior, with a Fermi liquid recovered under magnetic fields or high pressures. First-principles calculations identify competing nearest-neighbor (J_1) and next-nearest-neighbor (J_2) exchange interactions, with $J_2/J_1 \sim -0.5$, pointing to strong magnetic frustration. The interaction frustration is reduced, and magnetically ordered phases are stabilized upon the application of negative or positive pressures. This work offers a rare example of zero-field, ambient pressure quantum criticality mainly driven by interaction frustration in a square lattice.

Quantum phase transitions represent a cornerstone of condensed matter physics, where materials exhibit drastic changes in their ground state at zero temperature, induced by variations in non-thermal control parameters, e.g., pressure, magnetic field, or chemical doping [1–4]. At the quantum critical point (QCP), continuous phase transitions are governed by quantum fluctuations, leading to the emergence of exotic material properties, including non-Fermi-liquid (NFL) behavior [5–7], heavy fermion behavior [8–11], and unconventional superconductivity [12–17]. The breakdown of Landau’s Fermi-liquid theory near QCPs underscores the significance of electron correlations and scale-invariant quantum fluctuations, challenging traditional notions of ordering and quasiparticle coherence [18, 19].

Quantum criticality (QC) in materials without fine-tuning of parameters can predominantly emerge from geometric frustrations [20–23]. Consequently, the suppression of conventional order by quantum fluctuations brings about unusual ground states, such as quantum spin liquids or valence-bond solids [24–33]. In contrast,

interaction-driven frustration in square lattices, where geometric frustration is inherently absent, seldom results in genuine QCPs, as these materials typically exhibit long-range magnetic order (LRMO) at lower temperatures [34–42]. At present, the interplay between interaction-driven frustration and QC in metallic square lattices remains insufficiently explored.

In this Letter, we report a new intermetallic compound, $\text{ThCr}_2\text{Ge}_2\text{C}$, hosting a Cr_2C square-planar lattice, where competing nearest-neighbor (NN) J_1 and next-nearest-neighbor (NNN) J_2 interactions with $J_2/J_1 \sim -0.5$ stabilize QCPs at zero-field and ambient pressure. Our experimental investigations reveal that $\text{ThCr}_2\text{Ge}_2\text{C}$ exhibits NFL behavior in its resistivity and specific heat, along with the absence of LRMO down to 70 mK. Under high pressures, which alleviate the underlying magnetic frustration, the NFL behavior disappears experimentally, along with the stabilization of magnetically ordered phases as revealed by the calculations. These findings indicate that $\text{ThCr}_2\text{Ge}_2\text{C}$ could serve as a model system for studying QC and possible spin-nematic phase in metallic frustrated magnets.

Single and polycrystalline crystals of $\text{ThCr}_2\text{Ge}_2\text{C}$ were synthesized using the arc-melting technique. Additional details regarding the experimental setup and theoretical calculations are provided in the Supplemental Mate-

* corresponding author: yiqianglin@zju.edu.cn

† corresponding author: ghcao@zju.edu.cn

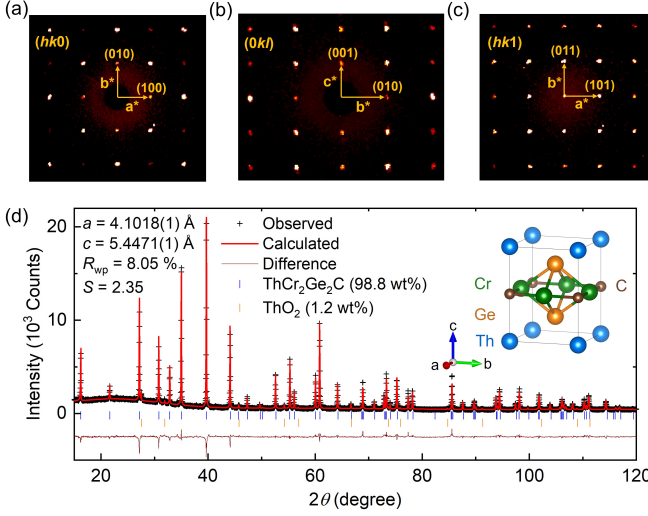


FIG. 1. (a-c) Reconstructed $\text{ThCr}_2\text{Ge}_2\text{C}$ single-crystal XRD patterns of $(hk0)$, $(0kl)$ and $(hk1)$ reflection planes, respectively. (d) Powder XRD at room temperature and its Rietveld refinement profile of $\text{ThCr}_2\text{Ge}_2\text{C}$. The inset shows the crystal structure of $\text{ThCr}_2\text{Ge}_2\text{C}$.

rials (SM) [43]. The single crystals were characterized via single-crystal X-ray diffractions (XRD) and energy dispersive X-ray spectroscopy (Fig. 1(a-c) and Fig. S1). The polycrystalline sample was analyzed by XRD at room temperature (Fig. 1(d)). The XRD results show that $\text{ThCr}_2\text{Ge}_2\text{C}$ crystallizes in a tetragonal lattice with space group $P4/mmm$ (Tables S1 and S2), where the Cr_2C square lattice adopts an anticonfiguration to the CuO_2 square net in cuprate superconductors (inset of Fig. 1(d)) [16].

Fig. 2(a) shows the temperature-dependence magnetic susceptibility $\chi(T)$ of the polycrystalline sample. As observed, a broad hump appears with its maximum at $T^* \approx 480 \text{ K}$. This feature, distinct from a sharp cusp or kink for antiferromagnetic (AFM) transition, is reminiscent of spin frustration, low-dimensional magnetism, or short-range correlations [44, 45]. The high-temperature data cannot be described by the extended Curie-Weiss formula, suggesting that AFM correlations persist up to 800 K. As a result, the Curie-Weiss temperature (θ_{CW}) is at least above 480 K, and the magnetic frustration index [46], $f = |\theta_{\text{CW}}|/T_N > 6850$ (T_N cannot be detected down to 70 mK, see below), turns out to be extraordinarily large, indicating extremely strong magnetic frustration [20].

The $\chi(T)$ of the single crystal shows a similar increasing trend to that of the polycrystalline sample above 100 K, demonstrating that these magnetic properties are intrinsic (Fig. 2(b)). The low-temperature $\chi(T)$ under a 10 Oe magnetic field shows no bifurcation in the zero-field-cooled (ZFC) and field-cooled (FC) data down to 2 K. Additionally, the ac susceptibility data show neither cusp-like anomaly nor frequency depen-

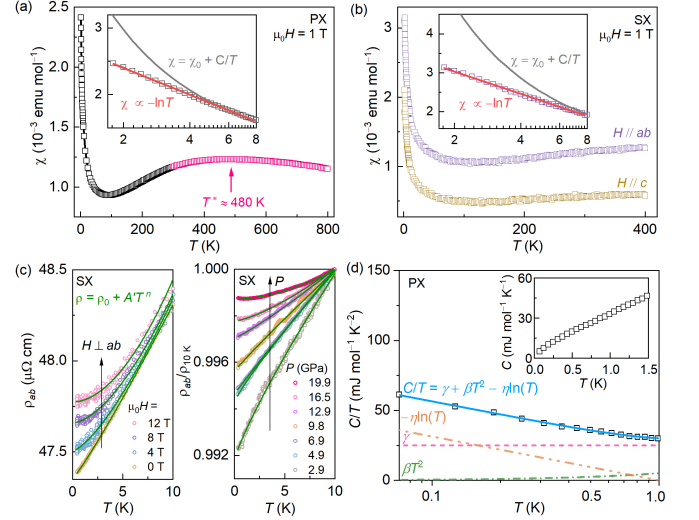


FIG. 2. (a) Temperature dependence of magnetic susceptibility, $\chi(T)$, for the polycrystalline $\text{ThCr}_2\text{Ge}_2\text{C}$ sample in a 1 T magnetic field. The data points in black were collected from 1.8 K to 300 K, and those in pink from 300 K to 800 K. The inset shows low-temperature $\chi(T)$. (b) $\chi(T)$ for a single crystal in a 1 T magnetic field, with the inset showing low-temperature $\chi(T)$. (c) Left panel is temperature dependence of the ab -plane electrical resistivity, $\rho_{ab}(T)$, for the single crystal under various magnetic fields applied perpendicular to the ab -plane. Right panel shows ρ_{ab}/ρ_{10K} under different pressures. The green lines show the low-temperature resistivity fitted with $\rho = \rho_0 + A'T^n$. (d) Plot of C/T versus T , with the blue line fitting $C/T = \gamma + \beta T^2 - \eta \ln(T)$. The dashed lines represent the contribution from each term. The inset shows the specific heat, $C(T)$, for the polycrystalline sample at low temperatures. PX denotes polycrystalline samples and SX denotes single crystals.

dence, ruling out the possibility of a spin-glass state in the system (Fig. S2). At low temperatures, both single and polycrystalline samples exhibit a $-\ln T$ dependence below 8 K, deviating from the Curie law (insets of Figs. 2(a,b)). This behavior is indicative of QC, due to strong quantum spin fluctuations [5, 24, 47].

The temperature dependence of electrical resistivity for the single crystal was measured under various magnetic fields and pressures (Fig. 2(c) and Figs. S3(a,b)). The low-temperature data ($45 \text{ mK} < T < 10 \text{ K}$) at zero-field and ambient pressure were fitted using the formula $\rho = \rho_0 + A'T^n$, yielding $\rho_0 = 47 \mu\Omega \text{ cm}$ and $n = 1.11$. The value of n is significantly smaller than 2.0, suggesting breakdown of the Fermi-liquid scenario. The NFL behavior may be induced by quantum critical fluctuations [5, 8, 10]. Similar fits to the data under magnetic fields and high pressures show an increase in n (Fig. S3(c)). Magnetic field or pressure can tune the quantum critical behavior, suppressing quantum fluctuations in the NFL state and driving the system to a Fermi liquid [48–52]. Assuming a Fermi-liquid scenario in the low-temperature limit, the data can alternatively be fit-

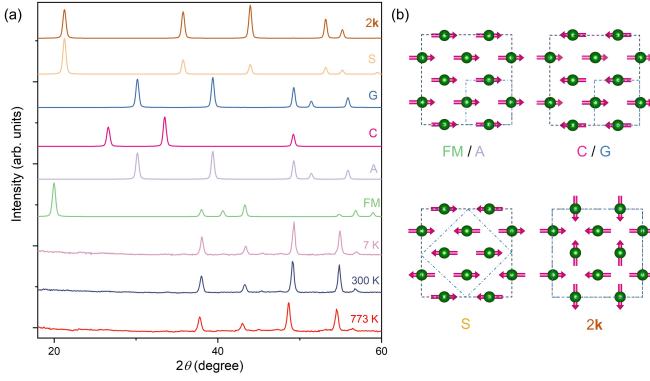


FIG. 3. (a) Simulated neutron powder diffraction (NPD) patterns for different magnetic structures, compared with NPD data for $\text{ThCr}_2\text{Ge}_2\text{C}$ at 7 K, 300 K, and 773 K. (b) Diagrams of magnetic structures with Cr spins aligned within the ab -plane: FM, C (ferromagnetic interlayer coupling), A, G, S, 2k (antiferromagnetic interlayer coupling). The blue dashed-dotted squares denote the magnetic unit cell for different magnetic structures.

ted using the formula $\rho = \rho_0 + AT^2$. The coefficient A under magnetic fields or pressures exhibits divergence as $\mu_0 H \rightarrow 0$ T or $P \rightarrow 0$ GPa (Fig. S3(d-f)), corroborating the presence of QC at zero field and ambient pressure [17, 51, 52].

The temperature dependence of the specific heat for the polycrystalline sample shows no obvious anomaly, indicating the absence of LRMO or short-range spin freezing down to 70 mK (inset of Fig. 2(d) and Fig. S4). Data in the temperature range of 70 mK to 1 K were well described by the formula $C/T = \gamma + \beta T^2 - \eta \ln(T)$ (Fig. 2(d)). The data fitting yields $\gamma = 24.98 \text{ mJ K}^{-2} \text{ mol}^{-1}$, which could be due to quasiparticle excitations in the residual “cold region” of the Fermi surface and/or other excitations like spinons [26, 29, 53]. Notably, C/T exhibits a $-\ln T$ dependence, which is not due to Schottky anomaly (inset of Fig. S4), but consistent with the quantum critical behavior observed in $\chi(T)$ and $\rho(T)$ [5, 48, 54].

Neutron powder diffraction (NPD) experiments were conducted to confirm the absence of LRMO (Fig. S5 and Table S2). Fig. 3 compares the simulated NPD patterns of the most likely magnetic structures (with Cr spins aligned within the ab -plane) to the experimental data at 7 K, 300 K, and 773 K [55–58]. No magnetic Bragg peaks were observed, only nuclear peaks, indicating the absence of LRMO down to 7 K. A comparison with Cr spins aligned along the c -axis yields the same result (Fig. S6). No additional peaks were found when comparing the 7 K and 300 K data with the 773 K data (well beyond $T^* \approx 480$ K), further supporting the absence of LRMO.

In square-lattice systems, where geometric frustration is absent, LRMO is typically suppressed by interaction frustration from competing NN and NNN exchange cou-

TABLE I. The spin exchange interaction constants, J_1 , J'_2 , J''_2 and J_z in $\text{ThCr}_2\text{Ge}_2\text{C}$. For $U = 1$ eV, J'_2 and J''_2 cannot be given separately. Therefore, we only provide an average value. The last column α is defined by $\alpha = (J'_2 + J''_2)/2J_1$.

U (eV)	J_i (meV/ S^2)				α
	J_1	J'_2	J''_2	J_z	
1	-74.94	31.41		0.72	-0.42
1.5	-27.99	36.37	-14.38	-0.79	-0.39
2	-17.67	43.73	-23.24	-4.22	-0.58

plings [59–62]. To reveal the magnetic frustration, we performed density functional theory (DFT)-based first-principles calculations (Fig. S7 and Table S3). Fig. 4(a) shows the calculated energy relative to the non-magnetic (NM) state E_m as a function of U for different magnetic configurations. The magnetic ground state evolves from A to FM, and then to S as the U value increases, with small energy differences ΔE_m between the ground state and other spin orders at each U value, indicating instability of the LRMO. To estimate interaction parameters in $\text{ThCr}_2\text{Ge}_2\text{C}$, we performed the constrained random-phase approximation (cRPA) calculations. The results give $U = 1.25$ eV and $J/U = 0.36$, close to those in the kagome metal CsCr_3Sb_5 [63]. Thus, a U value of about ~ 1 eV should be included to account for electron-electron interactions.

The exchange interactions between the Cr atoms can be calculated using a J_1 - J'_2 - J''_2 - J_z Heisenberg model (including a J_3 term yields nearly identical results, as detailed in the SM [43]). The effective magnetic interactions between Cr spins can be modeled by: (i) the NN coupling J_1 with direct Cr-Cr exchange, $\sim 70^\circ$ Cr-Ge-Cr superexchange, and 90° Cr-C-Cr superexchange, (ii) the NNN J'_2 with 180° Cr-C-Cr superexchange, (iii) the NNN J''_2 with $\sim 108^\circ$ Cr-Ge-Cr superexchange, and (iv) the interlayer NN coupling J_z , as shown in Fig. 4(b). Note that RKKY interactions, if not negligible, could also be included. The energies of the FM, A, C, G, S, and 2k magnetic states can be expressed as follows:

$$\begin{cases} E_{\text{FM}} - E_0 = 4J_1 + 2J'_2 + 2J''_2 + 2J_z, \\ E_{\text{A}} - E_0 = 4J_1 + 2J'_2 + 2J''_2 - 2J_z, \\ E_{\text{C}} - E_0 = -4J_1 + 2J'_2 + 2J''_2 + 2J_z, \\ E_{\text{G}} - E_0 = -4J_1 + 2J'_2 + 2J''_2 - 2J_z, \\ E_{\text{S}} - E_0 = -2J'_2 - 2J''_2 - 2J_z, \\ E_{2\text{k}} - E_0 = 2J'_2 - 2J''_2 - 2J_z, \end{cases}$$

where E_{FM} , E_{A} , E_{C} , E_{G} , E_{S} , and $E_{2\text{k}}$ denote the magnetic energy of those magnetic structures, respectively, and E_0 is an energy offset. The spin-exchange parameters, J_1 , J'_2 , J''_2 and J_z can be derived for $U \geq 1$ eV (for $U = 0$ and 0.5 eV, these values cannot be obtained, as the 2k state converges to a NM state), as listed in Table I. J_1 values are predominantly FM, with J'_2 always being AFM, and J''_2 being FM, all of which are consis-

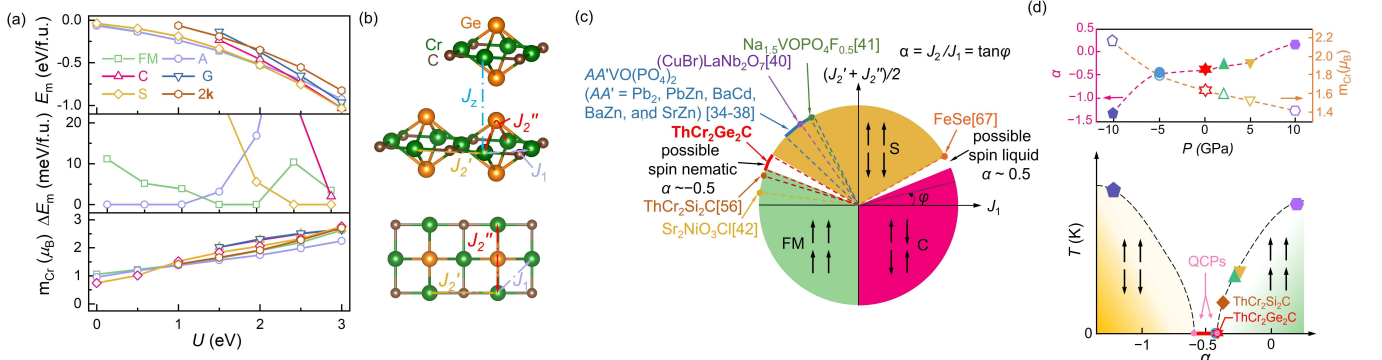


FIG. 4. (a) Calculation of the energy of $\text{ThCr}_2\text{Ge}_2\text{C}$ for different magnetic configurations and their corresponding magnetic moment of Cr. E_m represents the energy relative to non-magnetic configuration. ΔE_m is the energy difference between the magnetic ground state and other magnetic structures at each U value. (b) The magnetic exchange interactions between the Cr spins. (c) Modified phase diagram in the two-dimensional $J_1 - J_2$ model following Refs. [22, 36]. (d) The upper panel shows the pressure dependence of α (left axis) and magnetic moment (right axis) from DFT calculations, with the dashed lines as a guide to the eye. The lower panel presents the putative $T - \alpha$ phase diagram.

tent with the Goodenough-Kanamori rules [64–66]. J_z is about one order of magnitude smaller than J_1 , J_2' , and J_2'' , suggesting a quasi-two-dimensional (2D) magnetism in $\text{ThCr}_2\text{Ge}_2\text{C}$.

In a 2D scenario, there exist several phases as the ratio $\alpha = J_2/J_1 = \tan \varphi$ varies. Quantum fluctuations disrupt LRMO and result in the formation of two quantum critical regions at the boundaries of the ordered phases (Fig. 4(c)) [22, 36, 61]. A relevant example is the iron-chalcogenide superconductor FeSe , where quantum fluctuations associated with strongly frustrated interactions are identified as a potential trigger for the nematic quantum paramagnetic phase, interpolating between C- and S-type magnetic instabilities at $\alpha \sim 0.6$ [67–69]. For $\text{ThCr}_2\text{Ge}_2\text{C}$, the Cr_2C planes form a Lieb-like square-planar lattice, consisting of two Cr sites. One site has J_2' along the a axis and J_2'' along the b axis, while the other is the opposite. Therefore, the effective J_2 should be $(J_2' + J_2'')/2$, after taking the coordination number of Cr into account.

The result of $J_1 < 0$ and $(J_2' + J_2'')/2 > 0$ (Table I) indicates a spin-frustrated state in $\text{ThCr}_2\text{Ge}_2\text{C}$, which is commonly seen in square-lattice quantum magnets [34–42]. Remarkably, the value of $\alpha = (J_2' + J_2'')/2J_1$ is close to the maximal frustration, which could give rise to the possible spin nematic state as well as the substantial quantum fluctuations. Combined with experimental observations of NFL transport property, as well as logarithmic divergences in thermodynamic and magnetic susceptibilities, we propose that $\text{ThCr}_2\text{Ge}_2\text{C}$ could be a gapless quantum magnet near a QCP, induced by strong magnetic frustration (Fig. 4(d)).

To further address the above proposal, we performed DFT calculations to investigate the pressure effects on $\text{ThCr}_2\text{Ge}_2\text{C}$ at $U = 1.5$ eV (Fig. S9 and Table S5). The result indicates that the magnetic ground state evolves from an S-type structure under negative pres-

sure to a FM/A-type structure under positive pressure. Simultaneously, the value of α increases with pressure, showing a small change in the low-pressure range (± 5 GPa) and more significant changes at higher pressures (± 10 GPa) (Fig. 4(d)). Notably, the magnetic moment does not disappear in the quantum-critical regime, distinct from ordinary magnetic QC. For the isoelectronic analogue $\text{ThCr}_2\text{Si}_2\text{C}$, both NPD data and DFT calculations indicate an A-type magnetic ground state with in-plane FM ordering [56]. The substitution of Si for Ge induces a positive chemical pressure effect, consistent with the positive pressure effect calculated for $\text{ThCr}_2\text{Ge}_2\text{C}$. These findings strongly suggest that pressure may shift the system away from the quantum critical region and into a magnetically ordered state.

In summary, we report the discovery of $\text{ThCr}_2\text{Ge}_2\text{C}$, a metallic quantum magnet with a square-planar Cr lattice. Neither LRMO nor short-range spin freezing is detected by experiments down to 70 mK. DFT calculations reveal that the competition between J_1 and J_2 drives the QC. Thus, $\text{ThCr}_2\text{Ge}_2\text{C}$ could serve as a prototype for studying the role of competing interactions in QC. In-depth investigations utilizing techniques, such as muon spin relaxation, neutron scattering, and nuclear magnetic resonance, are expected to further address the QC and possible spin nematic phase in the future.

We acknowledge Jun Zhao for helpful discussions. This work was supported by the National Key Research and Development Program of China (2023YFA1406101, 2022YFA1403202), and the Natural Science Foundation of Shandong Province, China (ZR2023MA028).

Supplemental Materials: Quantum Criticality by Interaction Frustration in a Metallic Square-Planar Lattice

I. Contents

Experimental and computational methods

Fig. S1: Characterizations of $\text{ThCr}_2\text{Ge}_2\text{C}$ single crystals.

Fig. S2: Low-temperature dc and ac magnetic susceptibility of $\text{ThCr}_2\text{Ge}_2\text{C}$ single crystals.

Fig. S3: Temperature dependence of electrical resistivity for the single crystal of $\text{ThCr}_2\text{Ge}_2\text{C}$.

Fig. S4: Specific heat for the polycrystalline sample of $\text{ThCr}_2\text{Ge}_2\text{C}$.

Fig. S5: Neutron powder diffraction patterns of $\text{ThCr}_2\text{Ge}_2\text{C}$ at 7 K, 300 K and 773 K.

Fig. S6: Comparison of simulated neutron diffraction patterns with experimental data.

Fig. S7: Orbital-projected band structures and corresponding density of states of $\text{ThCr}_2\text{Ge}_2\text{C}$.

Fig. S8: Diagrams of the diagonal double stripe magnetic structure and the magnetic exchange interactions.

Fig. S9: DFT calculation results for $\text{ThCr}_2\text{Ge}_2\text{C}$ under positive and negative pressures.

Table S1: Crystallographic data for the single crystal $\text{ThCr}_2\text{Ge}_2\text{C}$ at 298 K.

Table S2: Refined results for $\text{ThCr}_2\text{Ge}_2\text{C}$ from X-ray and neutron powder diffractions at various temperatures.

Table S3: DFT calculation results for $\text{ThCr}_2\text{Ge}_2\text{C}$.

Table S4: Calculated spin exchange interactions and the α in $\text{ThCr}_2\text{Ge}_2\text{C}$ with J_3 term is included.

Table S5: DFT calculation results for $\text{ThCr}_2\text{Ge}_2\text{C}$ under positive and negative pressures.

II. Experimental and computational methods

The polycrystalline samples of $\text{ThCr}_2\text{Ge}_2\text{C}$ were synthesized using the powder of Th, Cr (99.95%), Ge (99.999%) and graphite (99.95%) as starting materials. The preparation of thorium metal was mentioned at Ref. [70]. The stoichiometric mixture of the materials was sufficiently mixed in an agate mortar and cold-pressed into a pellet. All these procedures were carried out in a glovebox filled with high-purity argon to prevent oxidation. The pellet was then melted in a water-cooled copper hearth by using an arc melting furnace. The sample was melted several times and flipped after each melting to ensure homogeneity. The arc-melted ingot was thoroughly ground, placed in an alumina crucible, sealed in an evacuated silica tube, and then heated to 1000 °C for two weeks. The single crystals of $\text{ThCr}_2\text{Ge}_2\text{C}$ were carefully extracted from the ingot obtained through the arc melting process.

Single-crystal X-ray diffraction (XRD) was carried on a Bruker D8 Venture diffractometer with Mo-K_α radiation. The data reduction was done using the commercial software package APEX4. The reconstructed images in the reciprocal space from the raw frames were produced using the reciprocal unit vectors of the tetragonal lattice by the software CrysAlis^{Pro} (CrysAlis Pro v.171.40.53, Rigaku Oxford Diffraction). The XRD for polycrystalline sample was performed at room temperature using a PANalytical X-ray diffractometer with $\text{Cu-K}_{\alpha 1}$ radiation. The chemical compositions of single crystals were confirmed by energy dispersive X-ray (EDX) spectroscopy (Oxford Instruments X-Max) equipped in a scanning electron microscope (SEM, Hitachi S-3700N). Neutron powder diffraction (NPD) measurements were carried out on the high-resolution neutron diffractometer at the Key Laboratory of Neutron Physics, Institute of Nuclear Physics and Chemistry, China Academy of Engineering Physics. The wavelength of the neutron was $\lambda = 1.8846 \text{ \AA}$. The crystal structure was refined by using the FullProf suite, with magnetic structures were analyzed with SARAH software [71, 72].

A standard four-terminal method was employed to measure the temperature-dependent resistivity. Resistivity measurements above 2.0 GPa were performed as described in Ref. [73], with details on the setup and methodology. The heat capacity was measured utilizing the standard relaxation method, using a Quantum Design physical property measurement system (PPMS) with dilution refrigerator inserts down to 70 mK. The magnetic properties were measured by a Quantum Design magnetic property measurement system (MPMS-3). The measurement was allowed at temperatures up to 800 K by employing a high-temperature option.

The first-principles calculations were done within the generalized gradient approximation (GGA) by using the Vienna Ab-initio Simulation Package (VASP) [74, 75]. We used the experimental crystal structure parameters for the initial relaxation. The forces were minimized to less than 0.0001 eV/Å in the relaxation. A plane-wave basis energy cutoff of 500 eV was employed alongside a $20 \times 20 \times 15$ Γ -centered K-mesh for DOS calculations. The Coulomb and exchange parameters, U and J , were introduced by using the GGA + U calculations, where the parameters U and J are not independent and the difference ($U_{\text{eff}} = U - J$) is meaningful. Considering NPD experimental results for $\text{ThCr}_2\text{Ge}_2\text{C}$, along with studies on other Th-based compounds such as ThB_2C [76], ThCr_2Si_2 [77], $\text{ThCr}_2\text{Si}_2\text{C}$ [56], all showing that Th does not carry a magnetic moment. Given that standard DFT calculations often overestimate the hybridization between f -electrons and conduction electrons, we fixed the U_{eff} at 11.0 eV for the Th $5f$ orbitals to mitigate this effect [56, 78].

To assess the relevance of long-range interactions, we evaluated the magnitude of the long-range interaction J_3 via calculating an additional magnetic structure, the diagonal double stripe (DDS) (Fig. S8), at $U = 1.5, 2 \text{ eV}$. The energy (E_m) of the DDS magnetic state, relative to the non-magnetic configuration, is -278.81 meV/f.u. and -489.31 meV/f.u. , respectively. Then the energies of the FM, A, C, G, S, $2\mathbf{k}$ and DDS magnetic states can be expressed as follows:

$$\begin{cases} E_{\text{FM}} - E_0 = 4J_1 + 2J'_2 + 2J''_2 + 4J_3 + 2J_z, \\ E_{\text{A}} - E_0 = 4J_1 + 2J'_2 + 2J''_2 + 4J_3 - 2J_z, \\ E_{\text{C}} - E_0 = -4J_1 + 2J'_2 + 2J''_2 + 4J_3 + 2J_z, \\ E_{\text{G}} - E_0 = -4J_1 + 2J'_2 + 2J''_2 + 4J_3 - 2J_z, \\ E_{\text{S}} - E_0 = -2J'_2 - 2J''_2 + 4J_3 - 2J_z, \\ E_{2\mathbf{k}} - E_0 = 2J'_2 - 2J''_2 - 4J_3 - 2J_z, \\ E_{\text{DDS}} - E_0 = -4J_3 - 2J_z, \end{cases}$$

The spin-exchange parameters derived are summarized in Table S4. The results show that J_3 is about one order of magnitude smaller than J_1 , J'_2 , and J''_2 , and that the α values remain nearly identical when J_3 is excluded.

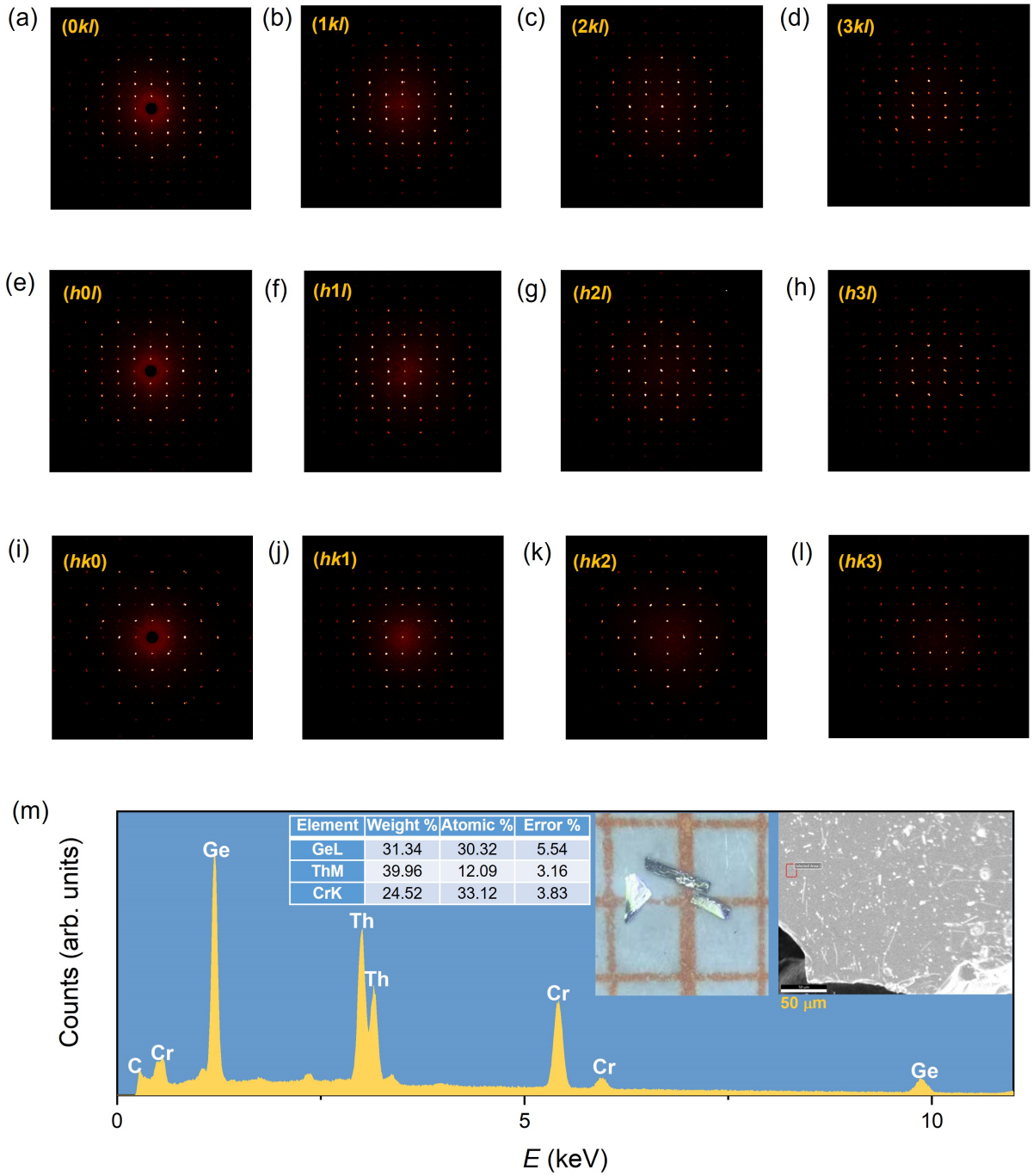


FIG. S1. (a-l) Reconstructed specific (hkl) planes of the $\text{ThCr}_2\text{Ge}_2\text{C}$ single crystal at 298 K. (m) The typical EDS spectrum of the $\text{ThCr}_2\text{Ge}_2\text{C}$ single crystal. The top-left inset shows the optical photograph, and the top-right inset shows an SEM image. The atomic ratios of Th, Cr, and Ge are in good agreement with the stoichiometry.

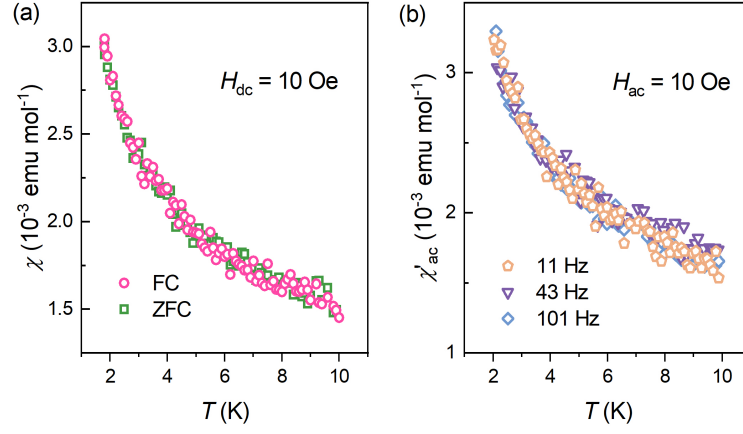


FIG. S2. (a) Low-temperature magnetic susceptibility of the ThCr₂Ge₂C single crystal with zero-field-cooling (ZFC) and field-cooling (FC) protocols under a 10 Oe magnetic field. (b) Real part of ac magnetic susceptibility at different oscillating frequencies under zero dc field.

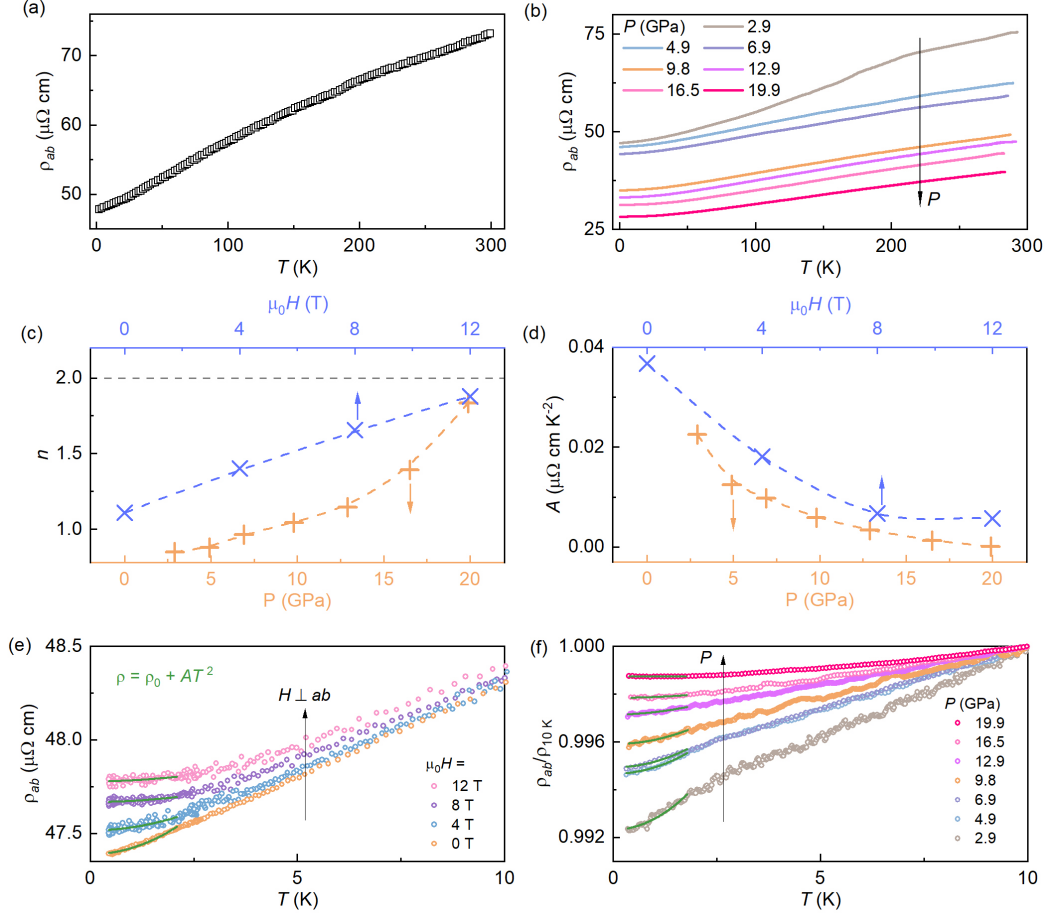


FIG. S3. (a) Temperature dependence of ab electrical resistivity, $\rho(T)$, for the ThCr₂Ge₂C single crystal. (b) $\rho_{ab}(T)$ of the single crystal under various pressures. (c) Power n as a function of magnetic field (upper axis) or pressure (lower axis). (d) Coefficients A as functions of magnetic field (upper axis) or pressure (lower axis). The dashed lines serve as a guide to the eye. (e, f) Fits of the ab -plane electrical resistivity under various magnetic fields applied perpendicular to the ab -plane and under different pressures, respectively, using the formula $\rho = \rho_0 + AT^2$.

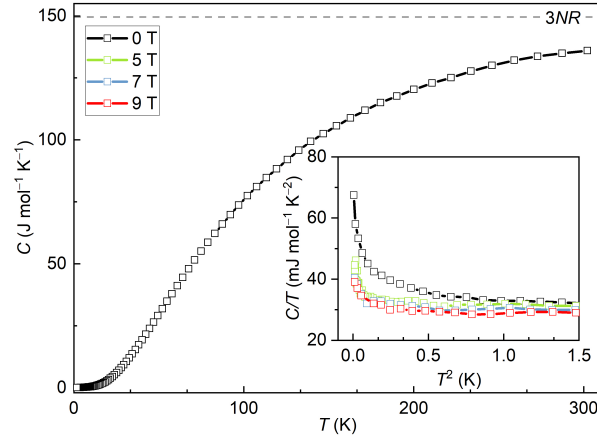


FIG. S4. Temperature dependence of the specific heat, $C(T)$, for the polycrystalline sample of $\text{ThCr}_2\text{Ge}_2\text{C}$. The inset plots C/T versus T^2 under magnetic fields of 0 T, 5 T, 7 T, and 9 T.

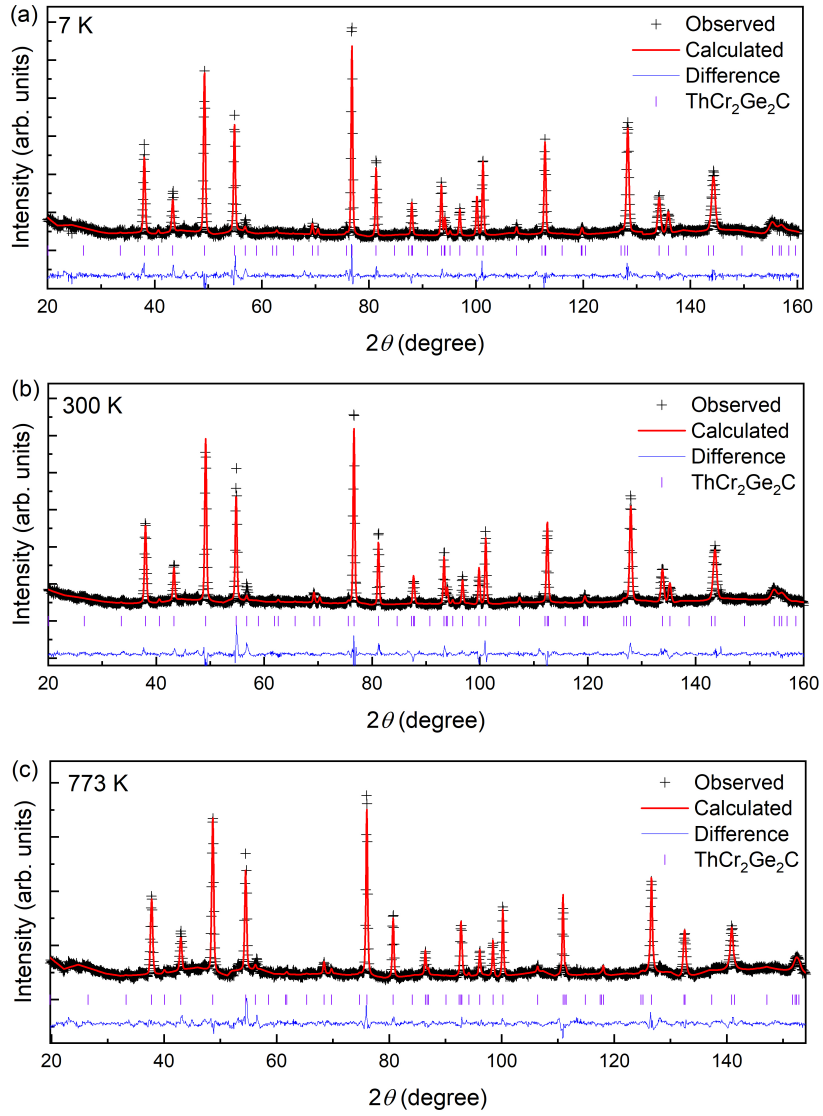


FIG. S5. The neutron powder diffraction patterns of $\text{ThCr}_2\text{Ge}_2\text{C}$ at 7 K (a), 300 K (b), and 773 K (c).

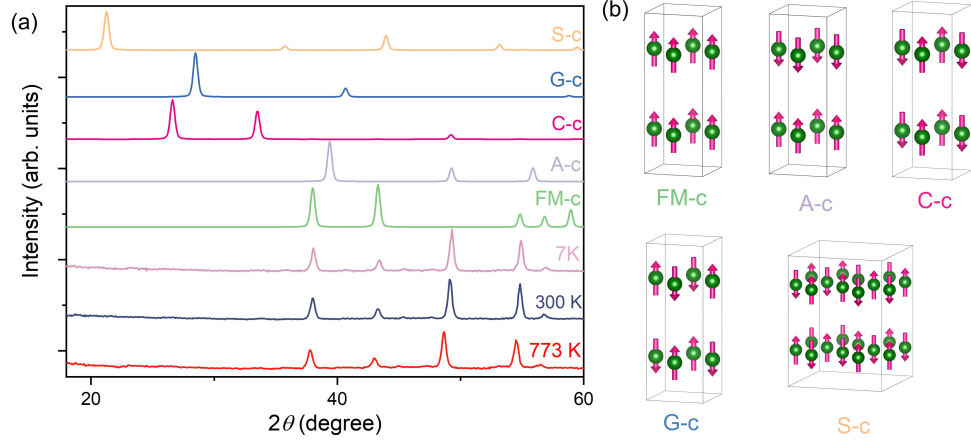


FIG. S6. (a) Simulated neutron diffraction patterns of different magnetic structures and experimental data for $\text{ThCr}_2\text{Ge}_2\text{C}$ measured at 7 K, 300 K, and 773 K. (b) Diagrams of different types of magnetic structures. The spins of Cr are aligned the c -axis.

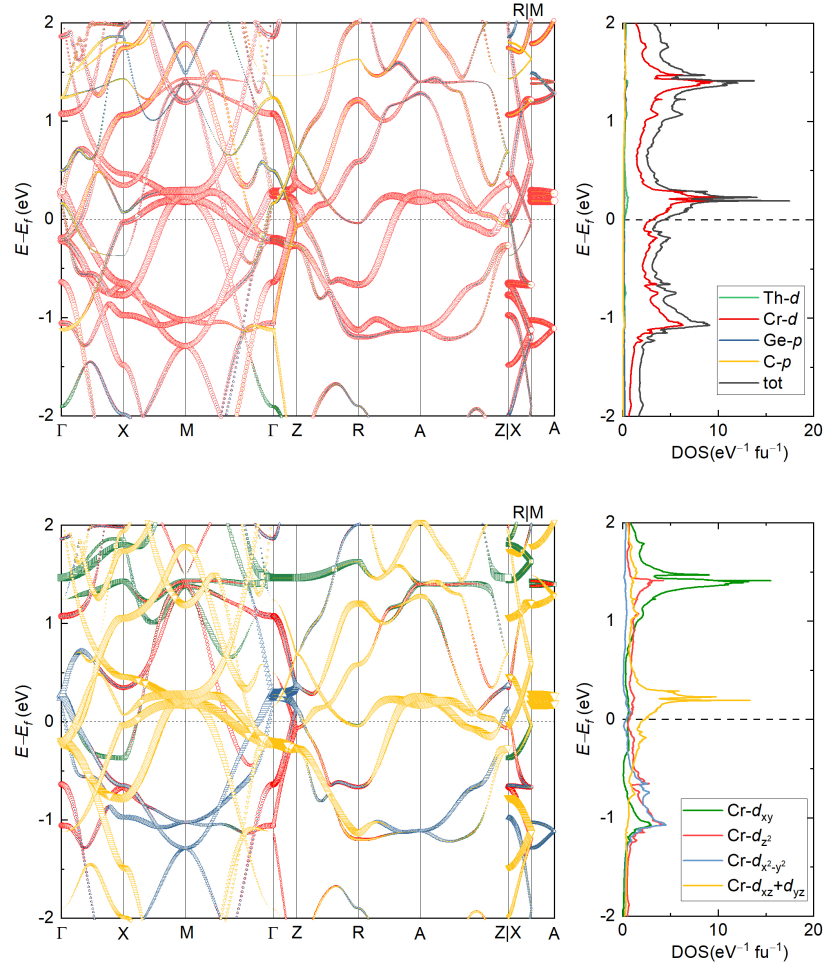


FIG. S7. (a) Orbital-projected band structure of $\text{ThCr}_2\text{Ge}_2\text{C}$ along high-symmetry paths. (b) The corresponding total and orbital-projected density of states (DOS) at $U = 1$ eV. (c) Projected band structure of Cr-3d orbitals in $\text{ThCr}_2\text{Ge}_2\text{C}$ along high-symmetry paths. (d) The corresponding projected DOS of Cr-3d orbitals at $U = 1$ eV.

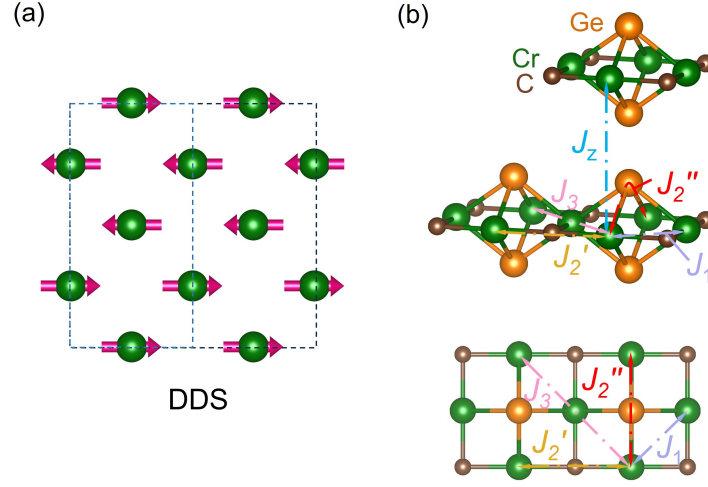


FIG. S8. (a) Diagram of the diagonal double stripe (DDS) magnetic structure with antiferromagnetic interlayer coupling, where the Cr spins are aligned within the ab -plane. The blue dashed-dotted square denotes the magnetic unit cell. (b) The magnetic exchange interactions between the Cr spins include an additional longer-range interaction, J_3 .

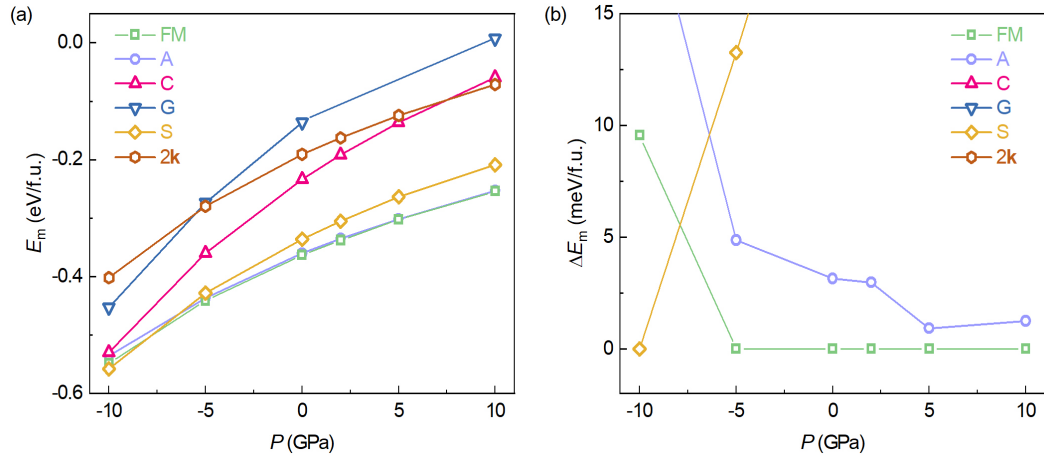


FIG. S9. (a) The calculated energy (E_m) relative to the non-magnetic configuration for different magnetic configurations of $\text{ThCr}_2\text{Ge}_2\text{C}$ under negative and positive pressures at $U = 1.5$ eV. (b) The calculated energy difference (ΔE_m) between the magnetic ground state and other magnetic structures at each pressure.

TABLE S2. Refined structural of ThCr₂Ge₂C from X-ray diffraction and neutron powder diffraction measurements at different temperatures.

Compound						ThCr ₂ Ge ₂ C					
Space group						<i>P4/mmm</i> (No. 123)					
Radiation			X-ray			Neutron					
Temperture			300 K			7 K			300 K		
<i>a</i> (Å)			4.1018(1)			4.0936(4)			4.1008(4)		
<i>c</i> (Å)			5.4471(1)			5.4317(6)			5.4480(6)		
<i>R</i> _{wp} (%)			8.05			7.88			7.08		
<i>R</i> _e (%)			3.42			4.06			3.90		
<i>S</i>			2.35			1.94			1.82		
Atom	site	<i>x</i>	<i>y</i>	<i>z</i>	<i>B</i> (Å ²)	<i>z</i>	<i>B</i> (Å ²)	<i>z</i>	<i>B</i> (Å ²)	<i>z</i>	<i>B</i> (Å ²)
Th	1 <i>a</i>	0	0	0	0.02(1)	0	0.3(1)	0	0.5(1)	0	0.3(1)
Cr	2 <i>e</i>	0.5	0	0.5	0.31(7)	0.5	0.4(1)	0.5	0.8(1)	0.5	1.0(1)
Ge	2 <i>h</i>	0.5	0.5	0.7724(4)	0.49(6)	0.7717(7)	0.04(9)	0.7712(7)	0.4(1)	0.7738(7)	0.3(1)
C	1 <i>b</i>	0	0	0.5	3.13(2)	0.5	0.7(1)	0.5	1.1(1)	0.5	1.5(2)

TABLE S3. The calculated magnetic energy E_m (in meV/f.u.) relative to the non-magnetic (NM) state and the corresponding magnetic moment μ_{Cr} (in μ_B) for different magnetic structures of ThCr₂Ge₂C. The magnetic ground state and its magnetic moment for each U value are emphasized in bold.

Magnetic structure	U (eV)													
	0.0		0.5		1.0		1.5		2.0		2.5		3.0	
	E_m	μ_{Cr}	E_m	μ_{Cr}	E_m	μ_{Cr}	E_m	μ_{Cr}	E_m	μ_{Cr}	E_m	μ_{Cr}	E_m	μ_{Cr}
FM	-53.80	1.05	-132.06	1.22	-232.99	1.40	-363.19	1.63	-530.78	1.90	-743.61	2.19	-1030.89	2.63
A	-64.95	0.95	-137.24	1.19	-236.85	1.37	-360.05	1.56	-513.92	1.74	-697.48	1.98	-926.16	2.25
C	Converge to FM		Converge to FM		Converge to FM		-233.25	2.02	-458.19	2.28	-727.93	2.50	-1032.32	2.66
G	Converge to A		Converge to A		Converge to A		-136.10	2.02	-372.57	2.31	-652.27	2.51	-965.34	2.66
S	-38.26	0.74	-98.20	1.02	-188.64	1.52	-336.03	1.83	-525.23	2.07	-753.97	2.32	-1034.34	2.77
2k	Converge to NM		Converge to NM		-62.71	1.42	-190.57	1.66	-350.29	1.92	-553.32	2.28	-826.26	2.71

TABLE S4. The calculated spin exchange interactions and the α ($= (J'_2 + J''_2)/2J_1$) values in ThCr₂Ge₂C for $U = 1.5$ and 2 eV, when the J_3 term is included.

U (eV)	J_i (meV/S ²)					α
	J_1	J'_2	J''_2	J_3	J_z	
1.5	-27.99	33.05	-11.07	-1.66	-0.79	-0.39
2	-17.67	45.00	-24.51	0.63	-4.22	-0.58

TABLE S5. The calculated magnetic energy E_m (in meV/f.u.) relative to the non-magnetic (NM) state and the corresponding magnetic moment μ_{Cr} (in μ_B) for different magnetic structures of $\text{ThCr}_2\text{Ge}_2\text{C}$ under positive and negative pressures at $U = 1.5$ eV. The magnetic ground state and its magnetic moment for each pressure are emphasized in bold. The last row α is defined by $\alpha = (J'_2 + J''_2)/2J_1$.

Magnetic structure	P (GPa)									
	-10.00		-5.00		2.00		5.00		10.00	
	E_m	μ_{Cr}	E_m	μ_{Cr}	E_m	μ_{Cr}	E_m	μ_{Cr}	E_m	μ_{Cr}
FM	-548.27	1.95	-441.33	1.81	-337.98	1.58	-302.43	1.52	-254.09	1.41
A	-536.01	1.81	-436.47	1.66	-335.00	1.51	-301.51	1.45	-252.84	1.38
C	-529.77	2.37	-360.29	2.20	-192.09	1.97	-136.54	1.88	-59.58	1.72
G	-452.79	2.37	-274.04	2.22	Converge to A		Converge to A		7.38	1.06
S	-557.82	2.17	-428.07	1.98	-305.44	1.78	-263.32	1.69	-208.77	1.52
2k	-402.06	2.09	-279.60	1.84	-162.89	1.60	-124.76	1.53	-71.58	1.41
J_1	-2.31		-10.13		-18.24		-20.74		-24.31	
J'_2	37.14		37.68		34.82		34.77		12.98	
J''_2	-31.18		-29.09		-24.79		-23.45		-21.31	
J_z	-3.07		-3.07		-0.75		-0.23		-0.32	
α	-1.29		-0.42		-0.28		-0.27		0.17	

-
- [1] S. Sachdev, Quantum phase transitions, *Phys. World* **12**, 33 (1999).
- [2] M. Vojta, Quantum phase transitions, *Rep. Prog. Phys.* **66**, 2069 (2003).
- [3] S. Sachdev, *Quantum magnetism and criticality*, Vol. 4 (Nature Publishing Group UK London, 2008) pp. 173–185.
- [4] S. Sachdev and B. Keimer, Quantum criticality, *Phys. Today* **64**, 29 (2011).
- [5] G. Stewart, Non-Fermi-liquid behavior in d - and f -electron metals, *Rev. Mod. Phys.* **73**, 797 (2001).
- [6] P. Coleman, C. Pépin, Q. Si, and R. Ramazashvili, How do Fermi liquids get heavy and die?, *J. Phys.:Condens. Matter* **13**, R723 (2001).
- [7] H. v. Löhneysen, A. Rosch, M. Vojta, and P. Wölfle, Fermi-liquid instabilities at magnetic quantum phase transitions, *Rev. Mod. Phys.* **79**, 1015 (2007).
- [8] N. Mathur, F. Grosche, S. Julian, I. Walker, D. Freye, R. Haselwimmer, and G. Lonzarich, Magnetically mediated superconductivity in heavy fermion compounds, *Nature* **394**, 39 (1998).
- [9] A. Schröder, G. Aeppli, R. Coldea, M. Adams, O. Stockert, H. Löhneysen, E. Bucher, R. Ramazashvili, and P. Coleman, Onset of antiferromagnetism in heavy-fermion metals, *Nature* **407**, 351 (2000).
- [10] J. Custers, P. Gegenwart, H. Wilhelm, K. Neumaier, Y. Tokiwa, O. Trovarelli, C. Geibel, F. Steglich, C. Pépin, and P. Coleman, The break-up of heavy electrons at a quantum critical point, *Nature* **424**, 524 (2003).
- [11] P. Gegenwart, Q. Si, and F. Steglich, Quantum criticality in heavy-fermion metals, *Nat. Phys.* **4**, 186 (2008).
- [12] D. C. Johnston, The puzzle of high temperature superconductivity in layered iron pnictides and chalcogenides, *Adv. Phys.* **59**, 803 (2010).
- [13] Q. Si and F. Steglich, Heavy fermions and quantum phase transitions, *Science* **329**, 1161 (2010).
- [14] P. Dai, J. Hu, and E. Dagotto, Magnetism and its microscopic origin in iron-based high-temperature superconductors, *Nat. Phys.* **8**, 709 (2012).
- [15] P. Dai, Antiferromagnetic order and spin dynamics in iron-based superconductors, *Rev. Mod. Phys.* **87**, 855 (2015).
- [16] B. Keimer, S. A. Kivelson, M. R. Norman, S. Uchida, and J. Zaanen, From quantum matter to high-temperature superconductivity in copper oxides, *Nature* **518**, 179 (2015).
- [17] Y. Liu, Z.-Y. Liu, J.-K. Bao, P.-T. Yang, L.-W. Ji, S.-Q. Wu, Q.-X. Shen, J. Luo, J. Yang, J.-Y. Liu, C.-C. Xu, W.-Z. Yang, W.-L. Chai, J.-Y. Lu, C.-C. Liu, B.-S. Wang, H. Jiang, Q. Tao, Z. Ren, X.-F. Xu, C. Cao, Z.-A. Xu, R. Zhou, J.-G. Cheng, and G.-H. Cao, Superconductivity under pressure in a chromium-based kagome metal, *Nature* **632**, 1032 (2024).
- [18] T. Senthil, L. Balents, S. Sachdev, A. Vishwanath, and M. P. Fisher, Quantum criticality beyond the Landau-Ginzburg-Wilson paradigm, *Phys. Rev. B* **70**, 144407 (2004).
- [19] C. Xu, Unconventional quantum critical points, *Int. J. Mod. Phys. B* **26**, 1230007 (2012).
- [20] L. Balents, Spin liquids in frustrated magnets, *Nature* **464**, 199 (2010).
- [21] Y. Zhou, K. Kanoda, and T.-K. Ng, Quantum spin liquid states, *Rev. Mod. Phys.* **89**, 025003 (2017).
- [22] B. Schmidt and P. Thalmeier, Frustrated two dimensional quantum magnets, *Phys. Rep.* **703**, 1 (2017).
- [23] M. Vojta, Frustration and quantum criticality, *Rep. Prog. Phys.* **81**, 064501 (2018).
- [24] S. Nakatsuji, Y. Machida, Y. Maeno, T. Tayama, T. Sakakibara, J. v. Duijn, L. Balicas, J. Millican, R. Macaluso, and J. Y. Chan, Metallic spin-liquid behavior of the geometrically frustrated Kondo lattice $\text{Pr}_2\text{Ir}_2\text{O}_7$, *Phys. Rev. Lett.* **96**, 087204 (2006).
- [25] Y. Okamoto, M. Nohara, H. Aruga-Katori, and H. Takagi, Spin-Liquid State in the $S = 1/2$ Hyperkagome Antiferromagnet $\text{Na}_4\text{Ir}_3\text{O}_8$, *Phys. Rev. Lett.* **99**, 137207 (2007).
- [26] S. Yamashita, Y. Nakazawa, M. Oguni, Y. Oshima, H. Nojiri, Y. Shimizu, K. Miyagawa, and K. Kanoda, Thermodynamic properties of a spin-1/2 spin-liquid state in a κ -type organic salt, *Nat. Phys.* **4**, 459 (2008).
- [27] T.-H. Han, J. S. Helton, S. Chu, D. G. Nocera, J. A. Rodriguez-Rivera, C. Broholm, and Y. S. Lee, Fractionalized excitations in the spin-liquid state of a kagome-lattice antiferromagnet, *Nature* **492**, 406 (2012).
- [28] Y. Tokiwa, J. Ishikawa, S. Nakatsuji, and P. Gegenwart, Quantum criticality in a metallic spin liquid, *Nat. Mater.* **13**, 356 (2014).
- [29] Y. Shen, Y.-D. Li, H. Wo, Y. Li, S. Shen, B. Pan, Q. Wang, H. C. Walker, P. Steffens, M. Boehm, Y. Hao, D. L. Quintero-Castro, L. W. Harriger, M. D. Frontzek, L. Hao, S. Meng, Q. Zhang, G. Chen, and J. Zhao, Evidence for a spinon fermi surface in a triangular-lattice quantum-spin-liquid candidate, *Nature* **540**, 559 (2016).
- [30] B. Gao, T. Chen, D. W. Tam, C.-L. Huang, K. Sasmal, D. T. Adroja, F. Ye, H. Cao, G. Sala, M. B. Stone, C. Baines, J. A. T. Verezhak, H. Hu, J.-H. Chung, X. Xu, S.-W. Cheong, M. Nallaiyan, S. Spagna, M. B. Maple, A. H. Nevidomskyy, E. Morosan, G. Chen, and P. Dai, Experimental signatures of a three-dimensional quantum spin liquid in effective spin-1/2 $\text{Ce}_2\text{Zr}_2\text{O}_7$ pyrochlore, *Nat. Phys.* **15**, 1052 (2019).
- [31] P.-L. Dai, G. Zhang, Y. Xie, C. Duan, Y. Gao, Z. Zhu, E. Feng, Z. Tao, C.-L. Huang, H. Cao, A. Podlesnyak, G. E. Granroth, M. S. Everett, J. C. Neufeind, D. Voneshen, S. Wang, G. Tan, E. Morosan, X. Wang, H.-Q. Lin, L. Shu, G. Chen, Y. Guo, X. Lu, and P. Dai, Spinon Fermi surface spin liquid in a triangular lattice antiferromagnet NaYbSe_2 , *Phys. Rev. X* **11**, 021044 (2021).
- [32] K. Matan, T. Ono, Y. Fukumoto, T. J. Sato, J. Yamaura, M. Yano, K. Morita, and H. Tanaka, Pinwheel valence-bond solid and triplet excitations in the two-dimensional deformed kagome lattice, *Nat. Phys.* **6**, 865 (2010).
- [33] J. P. Sheckelton, J. R. Neilson, D. G. Soltan, and T. M. McQueen, Possible valence-bond condensation in the frustrated cluster magnet $\text{LiZn}_2\text{Mo}_3\text{O}_8$, *Nat. Mater.* **11**, 493 (2012).
- [34] E. Kaul, H. Rosner, N. Shannon, R. Shpanchenko, and C. Geibel, Evidence for a frustrated square lattice with ferromagnetic nearest-neighbor interaction in the new compound $\text{Pb}_2\text{VO}(\text{PO}_4)_2$, *J. Magn. Magn. Mater.* **272**, 922 (2004).
- [35] R. Nath, A. Tsirlin, H. Rosner, and C. Geibel, Mag-

- netic properties of $\text{BaCdVO}(\text{PO}_4)_2$: A strongly frustrated spin-1/2 square lattice close to the quantum critical regime, *Phys. Rev. B* **78**, 064422 (2008).
- [36] R. Nath, Y. Furukawa, F. Borsa, E. Kaul, M. Baenitz, C. Geibel, and D. Johnston, Single-crystal ^{31}P NMR studies of the frustrated square-lattice compound $\text{Pb}_2(\text{VO})(\text{PO}_4)_2$, *Phys. Rev. B* **80**, 214430 (2009).
- [37] A. A. Tsirlin, R. Nath, A. M. Abakumov, R. V. Shpanchenko, C. Geibel, and H. Rosner, Frustrated square lattice with spatial anisotropy: Crystal structure and magnetic properties of $\text{PbZnVO}(\text{PO}_4)_2$, *Phys. Rev. B* **81**, 174424 (2010).
- [38] L. Bossoni, P. Carretta, R. Nath, M. Moscardini, M. Baenitz, and C. Geibel, NMR and μSR study of spin correlations in $\text{SrZnVO}(\text{PO}_4)_2$: An $S = 1/2$ frustrated magnet on a square lattice, *Phys. Rev. B* **83**, 014412 (2011).
- [39] H. Kageyama, T. Kitano, N. Oba, M. Nishi, S. Nagai, K. Hirota, L. Viciu, W. JB, J. Yasuda, Y. Baba, Y. Ajiro, and Y. K, Spin-Singlet Ground State in Two-Dimensional $S = 1/2$ Frustrated Square Lattice: $(\text{CuCl})\text{LaNb}_2\text{O}_7$, *J. Phys. Soc. Jpn.* **74**, 1702 (2005).
- [40] N. Oba, H. Kageyama, T. Kitano, J. Yasuda, Y. Baba, M. Nishi, K. Hirota, Y. Narumi, M. Hagiwara, K. Kindo, T. Saito, Y. Ajiro, and K. Yoshimura, Collinear order in frustrated quantum antiferromagnet on square lattice $(\text{CuBr})\text{LaNb}_2\text{O}_7$, *J. Phys. Soc. Jpn.* **75**, 113601 (2006).
- [41] A. A. Tsirlin, R. Nath, A. Abakumov, Y. Furukawa, D. Johnston, M. Hemmida, H.-A. Krug von Nidda, A. Loidl, C. Geibel, and H. Rosner, Phase separation and frustrated square lattice magnetism of $\text{Na}_{1.5}\text{VOPO}_4\text{F}_{0.5}$, *Phys. Rev. B* **84**, 014429 (2011).
- [42] Y. Tsujimoto, J. Sugiyama, M. Ochi, K. Kuroki, P. Manuel, D. D. Khalyavin, I. Umegaki, M. Månsson, D. Andreica, S. Hara, T. Sakurai, S. Okubo, H. Ohta, A. T. Boothroyd, and K. Yamaura, Impact of mixed anion ordered state on the magnetic ground states of $S = 1/2$ square-lattice quantum spin antiferromagnets, $\text{Sr}_2\text{NiO}_3\text{Cl}$ and $\text{Sr}_2\text{NiO}_3\text{F}$, *Phys. Rev. Mater.* **6**, 114404 (2022).
- [43] See Supplemental Materials for details.
- [44] A. Vasiliev, O. Volkova, E. Zvereva, and M. Markina, Milestones of low-D quantum magnetism, *npj Quantum Mater.* **3**, 18 (2018).
- [45] G.-M. Zhang, Y.-H. Su, Z.-Y. Lu, Z.-Y. Weng, D.-H. Lee, and T. Xiang, Universal linear-temperature dependence of static magnetic susceptibility in iron pnictides, *Europhys. Lett.* **86**, 37006 (2009).
- [46] A. Ramirez, Strongly geometrically frustrated magnets, *Annu. Rev. Mater. Sci.* **24**, 453 (1994).
- [47] S. Burdin, D. Grempel, and A. Georges, Heavy-fermion and spin-liquid behavior in a kondo lattice with magnetic frustration, *Phys. Rev. B* **66**, 045111 (2002).
- [48] H. Löhneysen, M. Sieck, O. Stockert, and M. Waffenschmidt, Investigation of non-Fermi-liquid behavior in $\text{CeCu}_{6-x}\text{Au}_x$, *Physica B* **223**, 471 (1996).
- [49] P. Gegenwart, J. Custers, C. Geibel, K. Neumaier, T. Tayama, K. Tenya, O. Trovarelli, and F. Steglich, Magnetic-field induced quantum critical point in YbRh_2Si_2 , *Phys. Rev. Lett.* **89**, 056402 (2002).
- [50] J. Paglione, M. Tanatar, D. Hawthorn, E. Boaknin, R. Hill, F. Ronning, M. Sutherland, L. Taillefer, C. Petrovic, and P. Canfield, Field-induced quantum critical point in CeCoIn_5 , *Phys. Rev. Lett.* **91**, 246405 (2003).
- [51] T. Shibauchi, L. Krusin-Elbaum, M. Hasegawa, Y. Kasa-hara, R. Okazaki, and Y. Matsuda, Field-induced quantum critical route to a Fermi liquid in high-temperature superconductors, *Proc. Natl. Acad. Sci.* **105**, 7120 (2008).
- [52] M. Pfeiffer, K. Semeniuk, J. F. Landaeta, R. Borth, C. Geibel, M. Nicklas, M. Brando, S. Khim, and E. Hassinger, Pressure-tuned quantum criticality in the locally noncentrosymmetric superconductor CeRh_2As_2 , *Phys. Rev. Lett.* **133**, 126506 (2024).
- [53] A. Rosch, Interplay of disorder and spin fluctuations in the resistivity near a quantum critical point, *Phys. Rev. Lett.* **82**, 4280 (1999).
- [54] T. Moriya and T. Takimoto, Anomalous properties around magnetic instability in heavy electron systems, *J. Phys. Soc. Jpn.* **64**, 960 (1995).
- [55] P. Lemoine, A. Verniere, M. Pasturel, G. Venturini, and B. Malaman, Unexpected magnetic ordering on the Cr substructure in $\text{UCr}_2\text{Si}_2\text{C}$ and structural relationships in quaternary U-Cr-Si-C compounds, *Inorg. Chem.* **57**, 2546 (2018).
- [56] Y. Xiao, B. Li, Q. Duan, S. Liu, Q. Ren, Y. Lin, Y. Xia, Y. Cui, H. Jiang, S. Wei, Z. Ren, Y. Mei, Y. Sun, S. Fu, S. Tan, Q. Jing, D. Yu, Y. Chen, C. Wang, and G. Cao, $\text{ThCr}_2\text{Si}_2\text{C}$: An Antiferromagnetic Metal with a Cr_2C Square Lattice, *Inorg. Chem.* **63**, 211 (2023).
- [57] F. Takeiri, Y. Matsumoto, T. Yamamoto, N. Hayashi, Z. Li, T. Tohyama, C. Tassel, C. Ritter, Y. Narumi, M. Hagiwara, and H. Kageyama, High-pressure synthesis of the layered iron oxyarsenide $\text{BaFe}_2\text{Se}_2\text{O}$ with strong magnetic anisotropy, *Phys. Rev. B* **94**, 184426 (2016).
- [58] S.-J. Song, Y.-Q. Lin, B.-Z. Li, S.-Q. Wu, Q.-Q. Zhu, Z. Ren, and G.-H. Cao, Tetragonal polymorph of $\text{BaFe}_2\text{S}_2\text{O}$ as an antiferromagnetic Mott insulator, *Phys. Rev. Mater.* **6**, 055002 (2022).
- [59] N. Shannon, B. Schmidt, K. Penc, and P. Thalmeier, Finite temperature properties and frustrated ferromagnetism in a square lattice Heisenberg model, *Eur. Phys. J. B.* **38**, 599 (2004).
- [60] N. Shannon, T. Momoi, and P. Sindzingre, Nematic order in square lattice frustrated ferromagnets, *Phys. Rev. Lett.* **96**, 027213 (2006).
- [61] J. Richter, R. Darradi, J. Schulenburg, D. J. J. Farnell, and H. Rosner, Frustrated spin-1/2 J_1 - J_2 Heisenberg ferromagnet on the square lattice studied via exact diagonalization and coupled-cluster method, *Phys. Rev. B* **81**, 174429 (2010).
- [62] J. Wen, S.-L. Yu, S. Li, W. Yu, and J.-X. Li, Experimental identification of quantum spin liquids, *npj Quantum Mater.* **4**, 12 (2019).
- [63] S. Wu, C. Xu, X. Wang, H.-Q. Lin, C. Cao, and G.-H. Cao, Flat-band enhanced antiferromagnetic fluctuations and superconductivity in pressurized CsCr_3Sb_5 , *Nat. Commun.* **16**, 1375 (2025).
- [64] J. B. Goodenough, Theory of the role of covalence in the perovskite-type manganites $[\text{La}, \text{M}(\text{II})]\text{MnO}_3$, *Phys. rev.* **100**, 564 (1955).
- [65] J. B. Goodenough, An interpretation of the magnetic properties of the perovskite-type mixed crystals $\text{La}_{1-x}\text{Sr}_x\text{CoO}_{3-\lambda}$, *J. Phys. Chem. Solids.* **6**, 287 (1958).
- [66] J. Kanamori, Theory of the magnetic properties of ferrous and cobaltous oxides, I, *Prog. Theor. Phys.* **17**, 177 (1957).
- [67] F. Wang, S. A. Kivelson, and D.-H. Lee, Nematicity and

- quantum paramagnetism in FeSe, *Nat. Phys.* **11**, 959 (2015).
- [68] Q. Wang, Y. Shen, B. Pan, X. Zhang, K. Ikeuchi, K. Iida, A. D. Christianson, H. C. Walker, D. T. Adroja, M. Abdel-Hafiez, X. Chen, D. A. Chareev, A. N. Vasiliev, and J. Zhao, Magnetic ground state of FeSe, *Nat. Commun.* **7**, 12182 (2016).
- [69] Q. Wang, Y. Shen, B. Pan, Y. Hao, M. Ma, F. Zhou, P. Steffens, K. Schmalzl, T. R. Forrest, M. Abdel-Hafiez, X. Chen, D. A. Chareev, A. N. Vasiliev, P. Bourges, Y. Sidis, H. Cao, and J. Zhao, Strong interplay between stripe spin fluctuations, nematicity and superconductivity in FeSe, *Nat. Mater.* **15**, 159 (2016).
- [70] C. Wang, Z.-C. Wang, Y.-X. Mei, Y.-K. Li, L. Li, Z.-T. Tang, Y. Liu, P. Zhang, H.-F. Zhai, Z.-A. Xu, and G.-H. Cao, A new ZrCuSiAs-type superconductor: ThFeAsN, *J. Am. Chem. Soc.* **138**, 2170 (2016).
- [71] J. Rodríguez-Carvajal, Recent advances in magnetic structure determination by neutron powder diffraction, *Physica B* **192**, 55 (1993).
- [72] A. Wills, A new protocol for the determination of magnetic structures using simulated annealing and representational analysis (SARAh), *Physica B* **276**, 680 (2000).
- [73] Y. Zhang, D. Su, Y. Huang, Z. Shan, H. Sun, M. Huo, K. Ye, J. Zhang, Z. Yang, Y. Xu, Y. Su, R. Li, M. Smidman, M. Wang, L. Jiao, and H. Yuan, High-temperature superconductivity with zero resistance and strange-metal behaviour in $\text{La}_3\text{Ni}_2\text{O}_{7-\delta}$, *Nat. Phys.* **20**, 1269 (2024).
- [74] J. P. Perdew, K. Burke, and M. Ernzerhof, Generalized gradient approximation made simple, *Phys. Rev. Lett.* **77**, 3865 (1996).
- [75] G. Kresse and J. Furthmüller, Efficient iterative schemes for ab initio total-energy calculations using a plane-wave basis set, *Phys. Rev. B* **54**, 11169 (1996).
- [76] P. Rogl and P. Fischer, Single-crystal X-ray and powder neutron diffraction of ThB_2C (ThB_2C -type), *J. Solid State Chem.* **78**, 294 (1989).
- [77] A. Szytuła, B. Penc, M. Hofmann, and J. Przewoźnik, Antiferromagnetism of ThCr_2Si_2 , *Solid State Commun.* **152**, 1027 (2012).
- [78] Z.-C. Wang, Y.-T. Shao, Y.-Q. Lin, S.-J. Song, B.-Z. Li, E.-J. Cheng, S.-Y. Li, Q.-Q. Zhu, Z. Ren, and G.-H. Cao, Absence of superconductivity in electron-doped chromium pnictides $\text{ThCrAsN}_{1-x}\text{O}_x$, *Phys. Rev. B* **108**, 064503 (2023).